

# Finite-momentum superconductivity with singlet-triplet mixing in an altermagnetic metal: A pairing instability analysis

Hui Hu,<sup>1,\*</sup> Zhao Liu,<sup>1</sup> Jia Wang,<sup>1</sup> Xia-Ji Liu,<sup>1</sup> and Yoji Ohashi<sup>2,†</sup>

<sup>1</sup>*Centre for Quantum Technology Theory, Swinburne University of Technology, Melbourne 3122, Australia*

<sup>2</sup>*Department of Physics, Keio University, Yokohama, Kanagawa 223-8522, Japan*

(Dated: March 16, 2026)

We analyze the pairing instability of an altermagnetic metal on a square lattice driven by an attractive nearest-neighbor interaction. This interaction enables multiple pairing channels, including even-parity extended  $s$ -wave and  $d$ -wave states, as well as two odd-parity  $p$ -wave channels. We verify that altermagnetic spin-splitting in the single-particle dispersion gives rise to finite-momentum pairing between electrons with unlike spins, in agreement with earlier predictions. Quite unexpectedly, this pairing typically emerges across multiple channels with mixed parity. Consequently, the resulting finite-momentum Fulde–Ferrell–Larkin–Ovchinnikov (FFLO) superconducting phase is expected to exhibit a multi-component order parameter featuring singlet-triplet mixing. We examine several forms of altermagnetism, specifically  $d_{xy}$ -wave and  $d_{x^2-y^2}$ -wave altermagnetic couplings, and present the corresponding phase diagrams. Additionally, we investigate the triplet pairing between electrons with identical spins, and find that it consistently occurs at zero center-of-mass momentum and is unfavorable at weak altermagnetic coupling and low electron filling. The influence of on-site attractive interactions on mixed-parity pairing is also explored.

## I. INTRODUCTION

A newly identified magnetic order, altermagnetism, has rapidly emerged as a subject of intense interest<sup>1–4</sup>. It transcends the conventional classification into ferromagnetic and antiferromagnetic phase by combining zero net magnetization with a momentum-dependent spin splitting of electronic bands<sup>5–14</sup>. This spin polarization is enforced by crystalline symmetries rather than relativistic spin-orbit coupling<sup>1,15–17</sup>, leading to spin-resolved Fermi surfaces in the absence of macroscopic magnetic fields. As a result, altermagnets occupy a unique position among magnetically ordered quantum materials<sup>1–4</sup>. Experimental signatures of altermagnetism have now been reported in an increasing number of compounds<sup>18–21</sup>, underscoring its relevance as a generic and robust form of magnetic order.

Spin-split Fermi surfaces in the absence of net magnetization have profound implications for quantum many-body phenomena<sup>3,4,22,23</sup>, including superconductivity<sup>24–49</sup>. The intrinsic spin imbalance imposed by altermagnetic order strongly constrains Cooper pairing and favors unconventional superconducting states<sup>22</sup>. Unlike ferromagnetic superconductors, where uniform spin splitting tends to suppress singlet pairing, the momentum-dependent spin polarization in altermagnets permits symmetry-compatible pairing channels that remain robust over a wide parameter range. A natural consequence of this spin-resolved electronic structure is the emergence of finite-momentum Cooper pairing<sup>25,30,31,35–38,40–45</sup>, closely analogous to the Fulde–Ferrell–Larkin–Ovchinnikov (FFLO) state originally proposed for Zeeman-field-driven superconductors<sup>50–63</sup>, where pairing at finite center-of-mass momentum leads to a spatially modulated order parameter. Despite extensive efforts, such FFLO states remain fragile

in conventional settings due to orbital depairing and competing instabilities<sup>64–66</sup>.

Altermagnets provide a qualitatively different route to FFLO superconductivity, in which finite-momentum pairing is stabilized by symmetry-enforced spin splitting rather than external magnetic fields<sup>67</sup>. This eliminates orbital pair breaking and directly ties the modulation wave vector to crystal symmetry, rendering FFLO-like states intrinsic and potentially robust. The resulting interplay between altermagnetism and finite-momentum pairing establishes altermagnetic superconductors as a promising platform for realizing spatially modulated superconductivity and for exploring the role of magnetic symmetry in unconventional pairing<sup>4</sup>.

To date, altermagnetism-induced FFLO superconductivity has been explored primarily through theoretical studies based on two-dimensional lattice Hamiltonians with either on-site<sup>36,38,40,47</sup> or nearest-neighbor<sup>31,35,38,45</sup> attractive interactions. The on-site attraction case is comparatively straightforward, as it supports a single  $s$ -wave pairing channel. In this setting, the physical mechanism underlying FFLO formation is most transparently revealed within a low-filling continuum description<sup>30,41,43,47</sup>: sufficiently strong altermagnetic coupling induces a continuous transition from conventional Bardeen–Cooper–Schrieffer (BCS) pairing to an inhomogeneous FFLO state, giving rise to rich phase diagrams under magnetic field featuring quantum Lifshitz multi-critical points separating polarized BCS, FFLO, and normal phases.

By contrast, nearest-neighbor attraction presents a more intricate situation, since it supports multiple competing pairing channels<sup>27,38,48</sup>, including extended  $s$ -wave, two  $p$ -wave, and  $d$ -wave pairings. In the absence of spin-orbit coupling, most mean-field studies restrict attention to a single dominant channel, assuming either spin-singlet ( $s$ - or  $d$ -wave) or spin-triplet ( $p$ -wave) pair-

ing. Early works focused on topological  $p$ -wave superconductivity and its competition with  $s$ -wave order<sup>27</sup>, followed by investigations of  $d$ -wave FFLO superconductivity with and without external magnetic fields<sup>31</sup>. A notable exception is the recent work by Jasiewicz *et al.*<sup>45</sup>, who demonstrated singlet-triplet mixing with coexisting  $d$ -wave and  $p$ -wave FFLO pairings induced by  $d_{x^2-y^2}$ -type altermagnetism at relatively high electron filling. This result is further corroborated by an exact two-electron analysis<sup>48</sup>, showing that altermagnetism stabilizes bound pairs with finite center-of-mass momentum, whose ground state consists of a coherent superposition of spin-singlet and spin-triplet components.

In this work, we present a systematic study of singlet-triplet mixing in Cooper pairing within altermagnetic metals over a wide range of electron fillings and for different altermagnetic symmetries. To circumvent the numerical complexity associated with solving for multi-component superconducting order parameters, we employ a pairing-instability analysis for two electrons near the spin-split Fermi surfaces based on the Thouless criterion<sup>68,69</sup>. This approach naturally extends the earlier exact two-body calculations<sup>48</sup> by incorporating many-body effects arising from the presence of a Fermi sea<sup>70</sup>. We find that the leading pairing instability generically occurs at finite center-of-mass momentum and simultaneously involves spin-singlet and spin-triplet channels with mixed parity. Consequently, the superconducting phase is anticipated to host an FFLO state described by a multicomponent order parameter with intrinsic singlet-triplet mixing<sup>45</sup>. We determine the superconducting phase diagrams and quantify the relative

weights of the distinct pairing channels at the superconducting transition, as functions of electron filling and interaction strength for various types of altermagnetism.

The rest of this paper is organized as follows. In Sec. II, we introduce the model Hamiltonian. Section III formulates the many-body  $T$ -matrix approximation for the two-particle vertex function in the Cooper pairing channel and describes the procedure for identifying the leading pairing instability from the matrix structure of the vertex function. In Sec. IV, we examine the instability of opposite-spin Cooper pairing as a function of electron filling, considering separately the  $d_{xy}$ -wave and  $d_{x^2-y^2}$ -wave altermagnetic couplings. Section V presents a comparison of our results with previous predictions of altermagnetism-induced FFLO states driven by nearest-neighbor attractive interactions. In Sec. VI, we discuss the  $p$ -wave pairing instability for same-spin electrons, which always occurs at zero center-of-mass momentum, and contrast it with the opposite-spin pairing case. Finally, Sec. VII summarizes our findings and outlines possible directions for future investigation. Appendix A details the spectral broadening procedure employed in the numerical evaluation of the pair propagators, and Appendix B summarizes the results obtained upon inclusion of an on-site attractive interaction.

## II. MODEL HAMILTONIAN

We consider a degenerate electron gas on a square lattice subject to  $d$ -wave altermagnetism. In the absence of an external magnetic field, the system can be modeled by a low-energy single-band Hamiltonian<sup>31,38,47</sup>,  $\mathcal{H} = \mathcal{H}_0 + \mathcal{H}_{\text{int}}$ , of the form,

$$\mathcal{H}_0 = \sum_{\mathbf{k}} \left[ (\xi_{\mathbf{k}} + J_{\mathbf{k}}) c_{\mathbf{k}\uparrow}^\dagger c_{\mathbf{k}\uparrow} + (\xi_{\mathbf{k}} - J_{\mathbf{k}}) c_{\mathbf{k}\downarrow}^\dagger c_{\mathbf{k}\downarrow} \right], \quad (1)$$

$$\mathcal{H}_{\text{int}} = \frac{1}{\mathcal{S}} \sum_{\mathbf{k}, \mathbf{k}', \mathbf{q}} V_{\uparrow\downarrow}(\mathbf{k}, \mathbf{k}') c_{\mathbf{k}+\frac{\mathbf{q}}{2}\uparrow}^\dagger c_{-\mathbf{k}+\frac{\mathbf{q}}{2}\downarrow}^\dagger c_{-\mathbf{k}'+\frac{\mathbf{q}}{2}\downarrow} c_{\mathbf{k}'+\frac{\mathbf{q}}{2}\uparrow} + \frac{1}{\mathcal{S}} \sum_{\mathbf{k}, \mathbf{k}', \mathbf{q}; \sigma} V_{\sigma}(\mathbf{k}, \mathbf{k}') c_{\mathbf{k}+\frac{\mathbf{q}}{2}\sigma}^\dagger c_{-\mathbf{k}+\frac{\mathbf{q}}{2}\sigma}^\dagger c_{-\mathbf{k}'+\frac{\mathbf{q}}{2}\sigma} c_{\mathbf{k}'+\frac{\mathbf{q}}{2}\sigma}, \quad (2)$$

where  $c_{\mathbf{k}\sigma}^\dagger$  and  $c_{\mathbf{k}\sigma}$  represent the creation and annihilation operators, respectively, for electrons with momentum  $\mathbf{k}$  and spin  $\sigma = \uparrow, \downarrow$ , and  $\mathcal{S} = L^2$  is the total number of the lattice sites for a  $L \times L$  square lattice with periodic boundary conditions.

In the non-interacting kinetic Hamiltonian  $\mathcal{H}_0$ , the single-particle dispersion is given by

$$\xi_{\mathbf{k}} \equiv -2t(\cos k_x + \cos k_y) - \mu, \quad (3)$$

which describes nearest-neighbor hopping with amplitude  $t$ ; the chemical potential  $\mu$  is determined by the electron filling factor  $\nu$ . The momentum-dependent spin-splitting  $J_{\mathbf{k}}$  originates from altermagnetism. We focus on

the two cases: (i)  $d_{xy}$ -wave altermagnetism<sup>38</sup>, for which

$$J_{\mathbf{k}} = \lambda \sin(k_x) \sin(k_y), \quad (4)$$

and (ii)  $d_{x^2-y^2}$ -wave altermagnetism<sup>31</sup>, where

$$J_{\mathbf{k}} = \frac{\lambda}{2} [\cos k_x - \cos k_y]. \quad (5)$$

For notational simplicity, throughout the paper we define  $\xi_{\mathbf{k}\uparrow} = \xi_{\mathbf{k}} + J_{\mathbf{k}}$  and  $\xi_{\mathbf{k}\downarrow} = \xi_{\mathbf{k}} - J_{\mathbf{k}}$ .

In the interaction Hamiltonian  $\mathcal{H}_{\text{int}}$ , we assume a short-range interaction potential and adopt the extended attractive Hubbard  $U$ - $V$  model, which incorporates both on-site ( $U$ ) and nearest-neighbor ( $V$  and  $V_{\sigma}$ ) pairing interaction terms<sup>38</sup>:

$$\begin{aligned} \mathcal{H}_{\text{int}} = & U \sum_i n_{i\uparrow} n_{i\downarrow} + V \sum_{i\delta} n_{i\uparrow} n_{i+\delta,\downarrow} \\ & + \frac{V_\sigma}{2} \sum_{i\delta} \sum_\sigma n_{i\sigma} n_{i+\delta,\sigma}, \end{aligned} \quad (6)$$

where  $\delta = \pm\hat{x}, \pm\hat{y}$  labels the four nearest neighbors, and  $n_{i\sigma} = c_{i\sigma}^\dagger c_{i\sigma}$  denotes the electron number operator at lattice site  $i$ . The on-site interaction acts only between spin-up and spin-down electrons due to the Pauli exclusion principle. In contrast, the nearest-neighbor interaction can occur between electrons with either opposite spins or identical spins, characterized by coupling strengths  $V_\sigma$  and  $V$ , respectively, which are generally distinct. This happens when the nearest-neighbor interaction effectively emerges from spin fluctuations in the limit of strong on-site electron-electron repulsion<sup>71,72</sup>.

By expressing the interaction Hamiltonian in momentum space using the standard Fourier transform, we obtain the momentum-dependent nearest-neighbor interaction strengths<sup>27,31,38</sup>:

$$\begin{aligned} V_{\uparrow\downarrow}(\mathbf{k}, \mathbf{k}') &= U + 2V [\cos(k_x - k'_x) + \cos(k_y - k'_y)] \\ V_\sigma(\mathbf{k}, \mathbf{k}') &= V_\sigma [\cos(k_x - k'_x) + \cos(k_y - k'_y)]. \end{aligned} \quad (7)$$

The on-site interaction  $U$  is purely  $s$ -wave and momentum-independent, while the nearest-neighbor interactions ( $V$  and  $V_\sigma$ ) display pronounced momentum dependence. These nearest-neighbor interactions can be decomposed into different symmetry channels - namely, extended  $s$ -wave, two  $p$ -wave, and  $d$ -wave channels - each of which can be expressed in a *separable* form<sup>27,38</sup>. For instance, in the case of opposite spins, we can rewrite,

$$V_{\uparrow\downarrow}(\mathbf{k}, \mathbf{k}') = \sum_{\eta=s, \text{es}, p+, p-, d} V_\eta f_\eta(\mathbf{k}) f_\eta^*(\mathbf{k}'), \quad (9)$$

where  $V_s = U$ ,  $V_{\text{es}} = V_{p+} = V_{p-} = V_d = V$ , and the form factors of different channels are given by,

$$f_s(\mathbf{k}) = 1, \quad (10)$$

$$f_{\text{es}}(\mathbf{k}) = \cos k_x + \cos k_y, \quad (11)$$

$$f_{p+}(\mathbf{k}) = \sin k_x + \sin k_y, \quad (12)$$

$$f_{p-}(\mathbf{k}) = \sin k_x - \sin k_y, \quad (13)$$

$$f_d(\mathbf{k}) = \cos k_x - \cos k_y. \quad (14)$$

We can clearly distinguish between the parity-even channel ( $\eta = s, \text{es}, d$ ) corresponding to spin-singlet pairing,

and the parity-odd channel ( $\eta = p+, p-$ ) corresponding to spin-triplet pairing. For the spin-triplet case, the form factors can alternatively be expressed in the more familiar chiral forms<sup>27,38</sup>, i.e.,  $f_{p+ip}(\mathbf{k}) = \sin k_x + i \sin k_y$  and  $f_{p-ip}(\mathbf{k}) = \sin k_x - i \sin k_y$ . These forms are not considered in the present study in order to avoid introducing complex numbers into the numerical calculations.

### III. NON-SELF-CONSISTENT $T$ -MATRIX THEORY AND THOULESS CRITERION

We seek to determine the pairing instability of the normal state for a given set of parameters, including the electron filling  $\nu$ , the interaction strengths  $U$ ,  $V$  and  $V_\sigma$ , and the alternating coupling  $\lambda$ . This can be conveniently analyzed using the Thouless criterion applied to the inverse two-particle vertex function  $\Gamma^{-1}(\mathbf{Q}, \omega = 0)$ . In the normal state, the inverse vertex function is negative, while in the superconducting phase it becomes positive. The superconducting phase transition occurs when it crosses zero<sup>68,69</sup>,

$$\max_{\{\mathbf{Q}\}} \Gamma^{-1}(\mathbf{Q}, \omega = 0) = 0. \quad (15)$$

If the maximum of the inverse vertex function takes place at a nonzero momentum  $\mathbf{Q} \neq 0$ , the normal state becomes unstable toward the formation of an inhomogeneous FFLO superconducting state.

We note that the vertex function is not necessarily a scalar quantity. When multiple pairing channels are present, it generally takes a matrix form. In such cases, one should consider the *largest* eigenvalue  $\gamma_1(\mathbf{Q})$  of the inverse vertex function matrix at zero frequency. Accordingly, in the Thouless criterion,  $\Gamma^{-1}(\mathbf{Q}, \omega = 0)$  is replaced by  $\gamma_1(\mathbf{Q})$ . In the following, we employ the standard non-self-consistent many-body  $T$ -matrix approach to evaluate the two-particle vertex function<sup>73</sup>.

#### A. Pairing between electrons with opposite spins

Restricting our attention first to pairing between electrons with *opposite* spins, we formally derive the equation for the vertex function  $\Gamma(\mathbf{k}, \mathbf{k}'; \mathbf{Q}, \omega)$  in the Cooperon channel within the ladder approximation. By summing the diagrams shown in Fig. 1, we obtain,

$$\Gamma(\mathbf{k}, \mathbf{k}'; \mathbf{Q}, \omega) = V_{\uparrow\downarrow}(\mathbf{k}, \mathbf{k}') - \sum_{\mathbf{k}''} V_{\uparrow\downarrow}(\mathbf{k}, \mathbf{k}'') G_{0\uparrow}\left(k'' + \frac{q}{2}\right) G_{0\downarrow}\left(-k'' + \frac{q}{2}\right) \Gamma(\mathbf{k}'', \mathbf{k}'; \mathbf{Q}, \omega), \quad (16)$$

where  $G_{0\uparrow}$  and  $G_{0\downarrow}$  denote the non-interacting single-particle Green's functions, which depend on the four momenta  $k'' \equiv \{\mathbf{k}'', i\omega_m\}$  and  $q \equiv \{\mathbf{Q}, i\nu_n \rightarrow \omega^+ \equiv \omega + i0^+\}$ . The summation  $\sum_{\mathbf{k}''} \equiv (k_B T / \mathcal{S}) \sum_{i\omega_m} \sum_{\mathbf{k}''}$  runs over both the spatial momentum and the (fermionic) Matsubara frequency  $\omega_m = (2m + 1)\pi k_B T$ , with integer  $m \in \mathbb{Z}$ . The

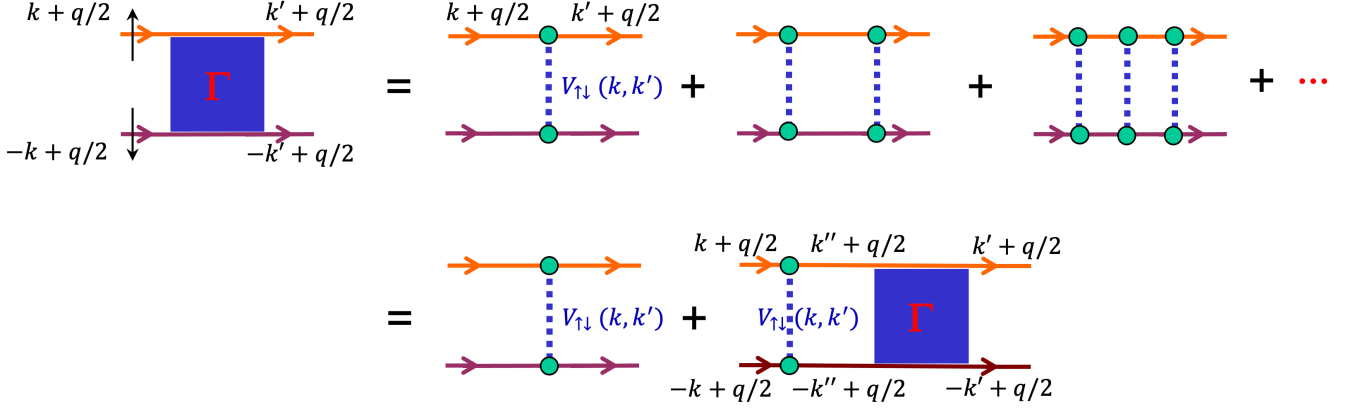


FIG. 1. Diagrammatic representation of the two-particle vertex function  $\Gamma(\mathbf{k}, \mathbf{k}'; \mathbf{Q}, \omega)$ , within the standard ladder approximation, for a general non-separable inter-particle interaction  $V_{\uparrow\downarrow}(\mathbf{k}, \mathbf{k}')$ .

summation over  $\omega_m$  can be performed straightforwardly<sup>73</sup>, yielding the expression,

$$\Gamma(\mathbf{k}, \mathbf{k}'; \mathbf{Q}, \omega) = V_{\uparrow\downarrow}(\mathbf{k}, \mathbf{k}') - \frac{1}{S} \sum_{\mathbf{k}''} V_{\uparrow\downarrow}(\mathbf{k}, \mathbf{k}'') \frac{[n_F(\xi_{\frac{\mathbf{Q}}{2} + \mathbf{k}''\uparrow}) + n_F(\xi_{\frac{\mathbf{Q}}{2} - \mathbf{k}''\downarrow}) - 1]}{\omega^+ - (\xi_{\frac{\mathbf{Q}}{2} + \mathbf{k}''\uparrow} + \xi_{\frac{\mathbf{Q}}{2} - \mathbf{k}''\downarrow})} \Gamma(\mathbf{k}'', \mathbf{k}'; \mathbf{Q}, \omega), \quad (17)$$

where  $n_F(x) \equiv 1/(e^{x/k_B T} + 1)$  is the Fermi-Dirac distribution function. In general, this equation is challenging to solve. However, by decomposing the interaction potential as in Eq. (9) into a total of  $N$  channels (with  $N = 5$  in the present case, corresponding to  $\eta = \text{s, es, p+, p-, d}$ , or equivalently  $\eta = 1, \dots, 5$ ),

$$V_{\uparrow\downarrow}(\mathbf{k}, \mathbf{k}') = [f_1(\mathbf{k}), \dots, f_\eta(\mathbf{k}), \dots, f_N(\mathbf{k})] \begin{bmatrix} V_1 & & & & \\ & \ddots & & & \\ & & V_\eta & & \\ & & & \ddots & \\ & & & & V_N \end{bmatrix} \begin{bmatrix} f_1^*(\mathbf{k}') \\ \vdots \\ f_\eta^*(\mathbf{k}') \\ \vdots \\ f_N^*(\mathbf{k}') \end{bmatrix}, \quad (18)$$

we may rewrite the vertex function in the form of,

$$\Gamma(\mathbf{k}, \mathbf{k}'; \mathbf{Q}, \omega) = [f_1(\mathbf{k}), \dots, f_\eta(\mathbf{k}), \dots, f_N(\mathbf{k})] \Gamma(\mathbf{Q}, \omega) \begin{bmatrix} f_1^*(\mathbf{k}') \\ \vdots \\ f_\eta^*(\mathbf{k}') \\ \vdots \\ f_N^*(\mathbf{k}') \end{bmatrix},$$

where  $\Gamma(\mathbf{Q}, \omega)$  is a  $N \times N$  matrix. Thus, by introducing a  $N \times N$  pair propagator matrix  $\chi(\mathbf{Q}, \omega)$ , whose matrix elements are given by

$$\chi_{\eta\eta'}(\mathbf{Q}, \omega) \equiv \frac{1}{S} \sum_{\mathbf{k}''} f_\eta^*(\mathbf{k}'') \frac{[n_F(\xi_{\frac{\mathbf{Q}}{2} + \mathbf{k}''\uparrow}) + n_F(\xi_{\frac{\mathbf{Q}}{2} - \mathbf{k}''\downarrow}) - 1]}{\omega^+ - (\xi_{\frac{\mathbf{Q}}{2} + \mathbf{k}''\uparrow} + \xi_{\frac{\mathbf{Q}}{2} - \mathbf{k}''\downarrow})} f_{\eta'}(\mathbf{k}''), \quad (19)$$

we can recast the vertex equation, Eq. (17), in matrix form for  $\Gamma(\mathbf{Q}, \omega)$ ,

$$\Gamma(\mathbf{Q}, \omega) = \mathbf{V} - \mathbf{V}\chi(\mathbf{Q}, \omega)\Gamma(\mathbf{Q}, \omega), \quad (20)$$

where the interaction matrix  $\mathbf{V} \equiv \text{diag}\{V_1, \dots, V_\eta, \dots, V_N\}$  is diagonal. It is readily seen that we can formally solve for the matrix of the inverse vertex function,

$$\mathbf{\Gamma}^{-1}(\mathbf{Q}, \omega) = \mathbf{V}^{-1} + \boldsymbol{\chi}(\mathbf{Q}, \omega) = \begin{bmatrix} V_1^{-1} + \chi_{11}(\mathbf{Q}, \omega) & \cdots & \chi_{1\eta}(\mathbf{Q}, \omega) & \cdots & \chi_{1N}(\mathbf{Q}, \omega) \\ \vdots & \ddots & \cdots & \cdots & \vdots \\ \chi_{\eta 1}(\mathbf{Q}, \omega) & \cdots & V_\eta^{-1} + \chi_{\eta\eta}(\mathbf{Q}, \omega) & \cdots & \chi_{\eta N}(\mathbf{Q}, \omega) \\ \vdots & \cdots & \vdots & \ddots & \vdots \\ \chi_{N1}(\mathbf{Q}, \omega) & \cdots & \chi_{N\eta}(\mathbf{Q}, \omega) & \cdots & V_N^{-1} + \chi_{NN}(\mathbf{Q}, \omega) \end{bmatrix}. \quad (21)$$

If the off-diagonal elements  $\chi_{\eta \neq \eta'}(\mathbf{Q}, \omega = 0)$  are negligible, the different channels effectively decouple, and it suffices to select the channel with the largest diagonal element. In general, however, for each center-of-mass pairing momentum  $\mathbf{Q}$ , one must diagonalize the full matrix  $\mathbf{\Gamma}^{-1}(\mathbf{Q}, \omega = 0)$  to determine its largest eigenvalue, i.e.,  $\gamma_1(\mathbf{Q})$ , which identifies the *leading* pairing instability in the Thouless criterion Eq. (15). The associated eigenvector  $[M_1, \dots, M_\eta, \dots, M_N]^T$  then specifies the structure of the superconducting order parameter once the instability develops. The remaining eigenvalues of  $\mathbf{\Gamma}^{-1}(\mathbf{Q}, \omega = 0)$  are denoted by  $\gamma_n(\mathbf{Q})$ , ordered in decreasing magnitude for  $n = 2, \dots, N$ .

### B. Two-electron limit

At this stage, it is instructive to consider the two-electron limit, where the two Fermi surfaces are absent. This corresponds to omitting the two Fermi-Dirac distribution functions in the pair propagators of Eq. (19). By absorbing the chemical potential into the frequency and defining the energy  $E = \omega + 2\mu$ , we introduce

$$L_{\eta\eta'} \equiv -\chi_{\eta\eta'} = \frac{1}{S} \sum_{\mathbf{k}} \frac{f_\eta^*(\mathbf{k}) f_{\eta'}(\mathbf{k})}{E - (\varepsilon_{\frac{\mathbf{Q}}{2} + \mathbf{k}\uparrow} + \varepsilon_{\frac{\mathbf{Q}}{2} - \mathbf{k}\downarrow})}, \quad (22)$$

where  $\varepsilon_{\mathbf{k}\sigma} = \xi_{\mathbf{k}\sigma} + \mu$ . The inverse vertex matrix can then be written as,  $\mathbf{\Gamma}_{\eta\eta'}^{-1}(\mathbf{Q}, E) = -L_{\eta\eta'}(E) + V_\eta^{-1} \delta_{\eta\eta'}$ . Physically,  $\mathbf{\Gamma}_{\eta\eta'}(\mathbf{Q}, \omega)$  may be interpreted as the Green's function of a Cooper pair, whose poles correspond to quasi-bound states with energies measured relative to the Fermi surfaces. Therefore, in the two-electron limit, the zeros of  $\mathbf{\Gamma}_{\eta\eta'}^{-1}(\mathbf{Q}, E)$ , determined by the condition,

$$\det \left[ L_{\eta\eta'}(E) - \frac{\delta_{\eta\eta'}}{V_\eta} \right] = 0, \quad (23)$$

give rise to the energies of tightly bound Cooper pairs. This reproduces the central equation previously derived for the two-electron bound-state problem<sup>48</sup>.

Returning to the many-body case, condensation of these bound pairs occurs when the pair energy  $E$  approaches the pair chemical potential  $2\mu$ , i.e., when  $\omega = 0$ , provided that residual interactions between bound pairs are neglected and  $\mathbf{\Gamma}_{\eta\eta'}(\mathbf{Q}, \omega)$  is regarded as the Green's

function of noninteracting composite bosons<sup>73</sup>. In this way, the Thouless criterion naturally emerges, following the standard picture of Bose-Einstein condensation in an ideal Bose gas.

### C. Pairing with parallel spins

We now consider pairing between electrons with *identical* spins. In this situation, the symmetric spin-triplet structure in spin space requires the real-space wave function to have odd parity. Consequently, only the two  $p$ -wave channels in the interaction potential  $V_\sigma(\mathbf{k}, \mathbf{k}')$  contribute. Following an analogous many-body  $T$ -matrix procedure, we obtain the  $2 \times 2$  inverse vertex matrix,

$$\mathbf{\Gamma}_\sigma^{-1}(\mathbf{Q}, \omega) = \begin{bmatrix} V_\sigma^{-1} + \chi_{11}^\sigma & \chi_{12}^\sigma \\ \chi_{21}^\sigma & V_\sigma^{-1} + \chi_{22}^\sigma \end{bmatrix}, \quad (24)$$

where the indices  $\eta, \eta' = 1, 2$  now label the  $p+$  and  $p-$  channels, respectively. The pair propagator  $\chi_{\eta\eta'}^\sigma$  can again be evaluated using Eq. (19), but with the identical single-particle dispersion for the two electrons, namely either  $\xi_{\mathbf{Q}/2 \pm \mathbf{k}'\uparrow}$  or  $\xi_{\mathbf{Q}/2 \pm \mathbf{k}'\downarrow}$ .

## IV. LEADING PAIRING INSTABILITY

The numerical procedure for identifying the leading pairing instability from the vertex matrices, Eq. (21) and Eq. (24), is straightforward. The primary numerical difficulty arises when evaluating the pair propagator in Eq. (19). Specifically, when the denominator approaches zero, the integrand develops a sharp peak at low temperature. To regularize this feature, a small spectral broadening factor  $\eta$  is introduced. The final results are then extrapolated to the limit  $\eta = 0^+$  using a cubic fit. As examined in detail in Appendix A, this strategy is efficient and introduces only negligible numerical errors.

Unless otherwise specified, we perform our calculations at an effectively zero temperature,  $T = 0.01t$ , in order to smooth the sharp Fermi surfaces. We assume a negligible on-site attraction,  $U = -0.01t$ , along with nearest-neighbor attractions  $V = -1.5t$  and  $V_\sigma = -1.5t$ . The impact of varying the on-site attraction  $U$  on the pairing instability is discussed in Appendix B.

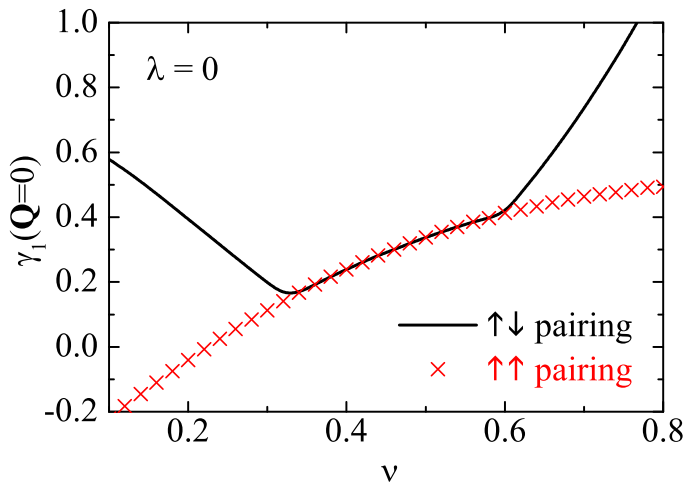


FIG. 2. The largest eigenvalue of the inverse vertex function matrix,  $\gamma_1(\mathbf{Q} = 0)$ , is plotted as a function of the lattice filling factor  $\nu$ , in the case without altermagnetism (i.e.,  $\lambda = 0$ ). The curves represent the results for pairing between electrons with unlike spins, while the red crosses indicate the triplet pairing results for spin-up electrons. Here and in the following figures, we adopt the interaction parameters  $U = -0.01t$  and  $V = V_\sigma = -1.5t$ , and temperature  $T = 0.01t$ , unless otherwise stated.

### A. The case without altermagnetism

We begin by analyzing the pairing instability in the absence of altermagnetism, where it consistently occurs at  $\mathbf{Q} = 0$ . In Fig. 2, we present the leading eigenvalue,  $\gamma_1(\mathbf{Q} = 0)$ , of the inverse vertex matrix  $\Gamma^{-1}$  for antiparallel spins (black solid line) and  $\Gamma_\sigma^{-1}$  for parallel spins (red crosses), plotted as a function of the electron filling factor  $\nu$ .

For antiparallel-spin pairing, the leading eigenvalue initially decreases with increasing  $\nu$ , then gradually rises around  $\nu \simeq 0.3$ , and eventually grows more steeply once  $\nu \gtrsim 0.6$ . This non-monotonic behavior reflects changes in the dominant pairing channel<sup>75</sup>. At low electron filling, the leading instability corresponds to an extended  $s$ -wave state. In the intermediate regime,  $0.3 \lesssim \nu \lesssim 0.6$ , it transitions to a  $p$ -wave state. Finally, for  $\nu \gtrsim 0.6$ , the pairing symmetry switches to  $d$ -wave. This interpretation is supported by the behavior of the leading eigenvalue for triplet  $p$ -wave pairing among spin-up electrons, which coincides in the intermediate filling range  $0.3 \lesssim \nu \lesssim 0.6$ , owing to the identical nearest-neighbor interaction strengths  $V = V_\sigma$ .

Notably, in the absence of altermagnetism, the leading eigenvalue for antiparallel-spin pairing is always at least as large as that for parallel-spin pairing. This indicates that parallel-spin pairing does not constitute the dominant instability for sufficiently small altermagnetic couplings when  $|V| \geq |V_\sigma|$ . Accordingly, in this section and the next, we focus on antiparallel-spin pairing. In the following, we separately discuss the two cases of the

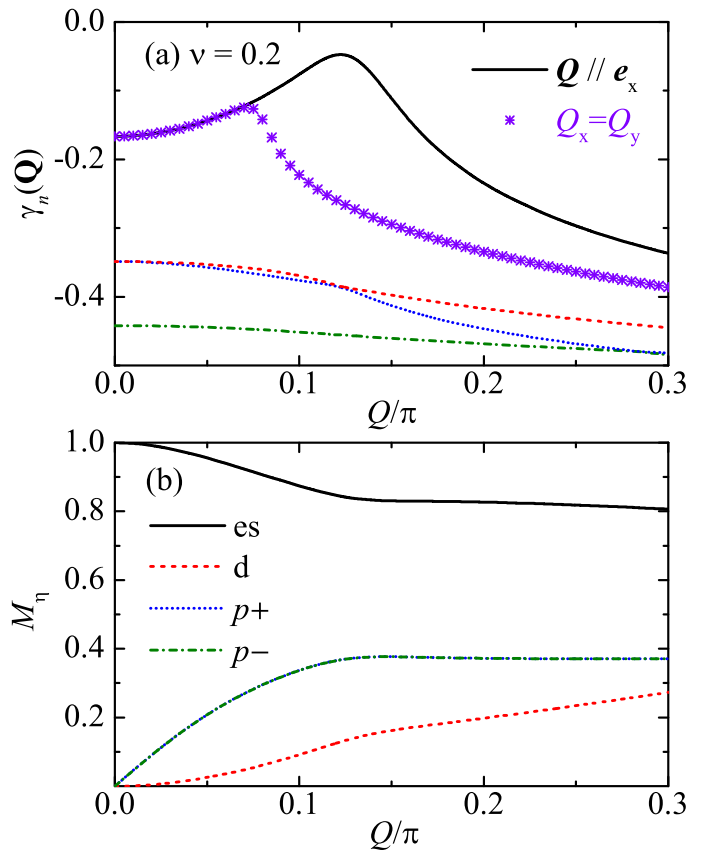


FIG. 3. (a) The curves represent the four eigenvalues of the inverse vertex function matrix,  $\gamma_n(\mathbf{Q})$ , at the filling factor  $\nu = 0.2$ , as a function of the center-of-mass momentum  $\mathbf{Q}$  when it lies along the  $x$ -axis. The crosses show  $\gamma_1(\mathbf{Q})$  for  $\mathbf{Q}$  directed along the diagonal ( $Q_x = Q_y$ ). In both orientations, introducing a  $d_{xy}$ -wave altermagnetic coupling with strength  $\lambda = 0.5t$  causes  $\gamma_1(\mathbf{Q})$  to peak at a nonzero  $\mathbf{Q}$ . (b) The eigenvectors associated with  $\gamma_1(\mathbf{Q})$  are shown for  $\mathbf{Q}$  along the  $x$ -axis.

$d_{xy}$ - and  $d_{x^2-y^2}$ -wave altermagnetism.

### B. $d_{xy}$ -wave altermagnetism

In Fig. 3(a), we report the eigenvalues of the inverse vertex matrix  $\gamma_n(\mathbf{Q})$  for a  $d_{xy}$ -wave altermagnetic coupling  $\lambda = 0.5t$  at low electron filling  $\nu = 0.2$ , plotted as a function of the center-of-mass momentum  $Q = |\mathbf{Q}|$  with  $\mathbf{Q}$  oriented along the  $x$ -direction. Only four eigenvalues are visible, since the fifth one - associated with the  $s$ -wave channel - lies far below the others due to the very weak on-site attraction  $U = -0.01t$ . The leading eigenvalue  $\gamma_1(\mathbf{Q})$  exhibits a pronounced maximum at a finite momentum  $Q \simeq 0.12\pi$ . For other directions of  $\mathbf{Q}$ ,  $\gamma_1(\mathbf{Q})$  likewise develops a local maximum at nonzero  $Q$ . The case where  $\mathbf{Q}$  points along the diagonal direction (i.e.,  $Q_x = Q_y$ ) is explicitly indicated in the figure by purple crosses. Nevertheless, in the presence of  $d_{xy}$ -

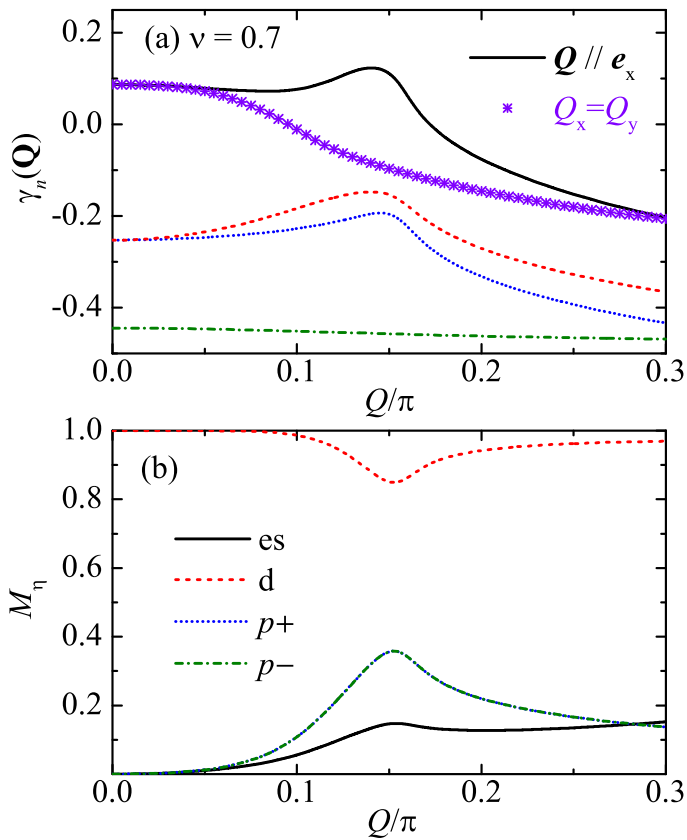


FIG. 4. The results are identical to that presented in Fig. 3, with the exception that they are calculated at a larger lattice filling factor of  $\nu = 0.7$ .

wave altermagnetism, the global maximum of the leading eigenvalue consistently occurs when  $\mathbf{Q}$  is aligned with the  $x$ -direction.

In general, the leading eigenvalue is associated with an eigenvector whose components  $M_\eta$  characterize the relative weight of different pairing channels in the dominant pairing instability. Figure 3(b) shows these components as a function of  $Q$ . At the peak momentum  $Q \simeq 0.12\pi$ , the extended  $s$ -wave channel clearly dominates, accompanied by two weaker degenerate  $p$ -wave contributions and only a negligible component from the  $d$ -wave channel.

At higher electron fillings, illustrated in Fig. 4 for the representative case  $\nu = 0.7$ , the leading eigenvalue of the inverse vertex matrix  $\gamma_1(\mathbf{Q})$  displays behavior qualitatively similar to that at low filling, but with two important differences. On the one hand, although the global maximum still happens at nonzero momentum when  $\mathbf{Q}$  directs along the  $x$ -direction, the point  $Q = 0$  now becomes a local maximum. This feature is especially evident when  $Q$  lies along the diagonal: in that case, the finite-momentum peak disappears entirely (see purple crosses). On the other hand, as the electron filling increases, the structure of the eigenvector associated with the leading eigenvalue changes dramatically. At the peak momentum  $Q \simeq 0.15\pi$ , the pairing instability is domi-

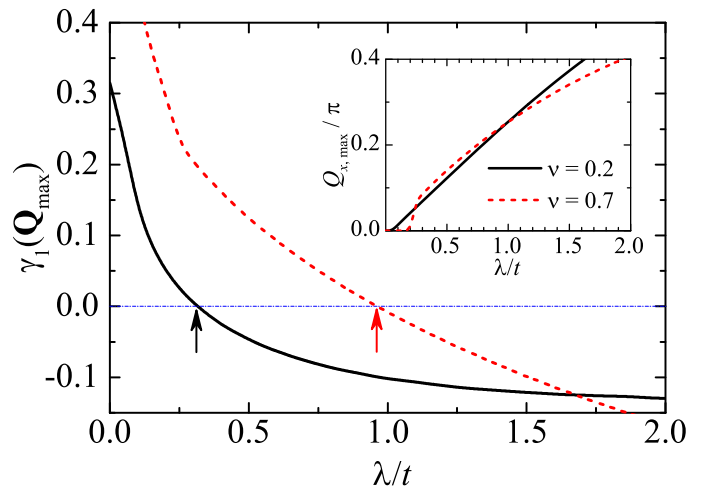


FIG. 5. The peak value of the dominant eigenvalue of the inverse vertex function matrix,  $\gamma_1(\mathbf{Q}_{\max})$ , is shown as a function of the  $d_{xy}$ -wave altermagnetic coupling strength  $\lambda$  for two lattice filling factors:  $\nu = 0.2$  (black solid line) and  $\nu = 0.7$  (red dashed line). The arrows highlight the critical altermagnetic coupling at which  $\gamma_1(\mathbf{Q}_{\max})$  vanishes. The inset shows the magnitude of the  $\mathbf{Q}$  vector at which this peak occurs.

nated by a  $d$ -wave component, followed by two degenerate  $p$ -wave channels, while the extended  $s$ -wave contribution becomes negligible. This evolution of the dominant pairing channel with increasing filling is consistent with the trend observed in the absence of altermagnetism, as previously shown in Fig. 2.

We have systematically repeated the numerical calculations for various values of altermagnetic couplings  $\lambda$  and electron fillings  $\nu$ , in order to determine the global maximum of the leading eigenvalue of the inverse vertex matrix  $\gamma_1(\mathbf{Q}_{\max})$ , the corresponding peak momentum  $\mathbf{Q}_{\max}$ , and the weights of the different pairing channels,  $W_\eta = |M_\eta|^2$ , obtained from the associated eigenvector at  $\mathbf{Q}_{\max}$ . In Fig. 5, we plot the global maximum as a function of  $\lambda$  for two representative filling factors:  $\nu = 0.2$  (black solid line) and  $\nu = 0.7$  (red dashed line), together with the corresponding peak momentum shown in the inset.

As  $\lambda$  increases,  $\gamma_1(\mathbf{Q}_{\max})$  generally decreases. This behavior can be understood from the fact that altermagnetism acts as a momentum-dependent effective magnetic field, which tends to suppress Cooper pairing. As a consequence, with increasing  $\lambda$ , the maximum may eventually reach zero at a critical altermagnetic coupling  $\lambda_c$ . According to the Thouless criterion Eq. (15), this critical point marks the boundary between the superconducting phase and the normal state. In the main panel, the critical couplings  $\lambda_c$  for  $\nu = 0.2$  and  $\nu = 0.7$  are indicated by black and red arrows, respectively. The inset further shows that the superconducting phase transition is always associated with a nonzero peak momentum,  $\mathbf{Q}_{\max} \neq 0$ . This demonstrates that the emergent superconducting phase corresponds to a finite-momentum

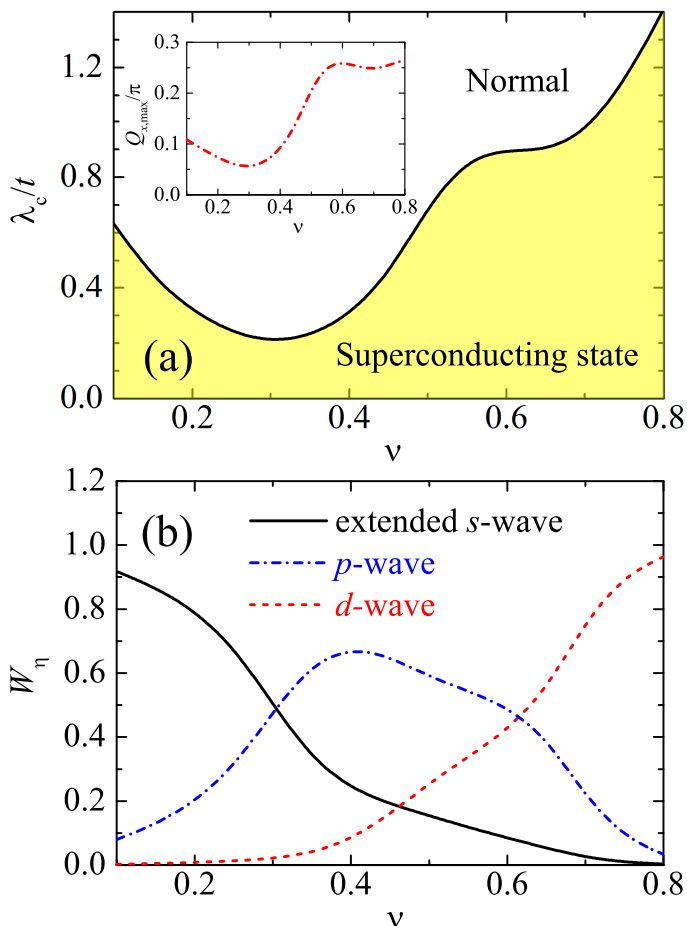


FIG. 6. (a) Phase diagram in the presence of  $d_{xy}$ -wave altermagnetism: the critical altermagnetic coupling strength  $\lambda_c$  is plotted as a function of the lattice filling factor  $\nu$ . The inset shows the center-of-mass momentum  $\mathbf{Q} = Q\mathbf{e}_x$  at the superconducting phase boundary. (b) Contribution of various partial-wave components to the leading pairing channel,  $W_\eta = |M_\eta|^2$ , is shown as a function of  $\nu$  at the superconducting transition.

FFLO state.

In Fig. 6(a), we present the critical altermagnetic coupling  $\lambda_c$  as a function of electron filling  $\nu$ , thereby establishing the corresponding phase diagram. The associated peak momentum  $Q_{\max}$  is displayed in the inset. Both  $\lambda_c$  and  $Q_{\max}$  show a similar non-monotonic dependence on  $\nu$ , closely resembling the behavior observed previously in Fig. 2 in the absence of altermagnetism. For instance, as  $\nu$  increases, the initially decreasing trend of  $\lambda_c$  reverses around  $\nu \simeq 0.3$ . Remarkably, this is precisely the filling at which - without altermagnetism - the dominant pairing channel switches from extended  $s$ -wave to  $p$ -wave symmetry. Furthermore,  $\lambda_c$  exhibits another change in slope and develops a plateau near  $\nu \simeq 0.6$ , where Fig. 2 indicates a transition of the dominant pairing channel from  $p$ -wave to  $d$ -wave character.

Motivated by this correspondence, it is natural to relate the non-monotonic  $\nu$ -dependence of  $\lambda_c$  to changes

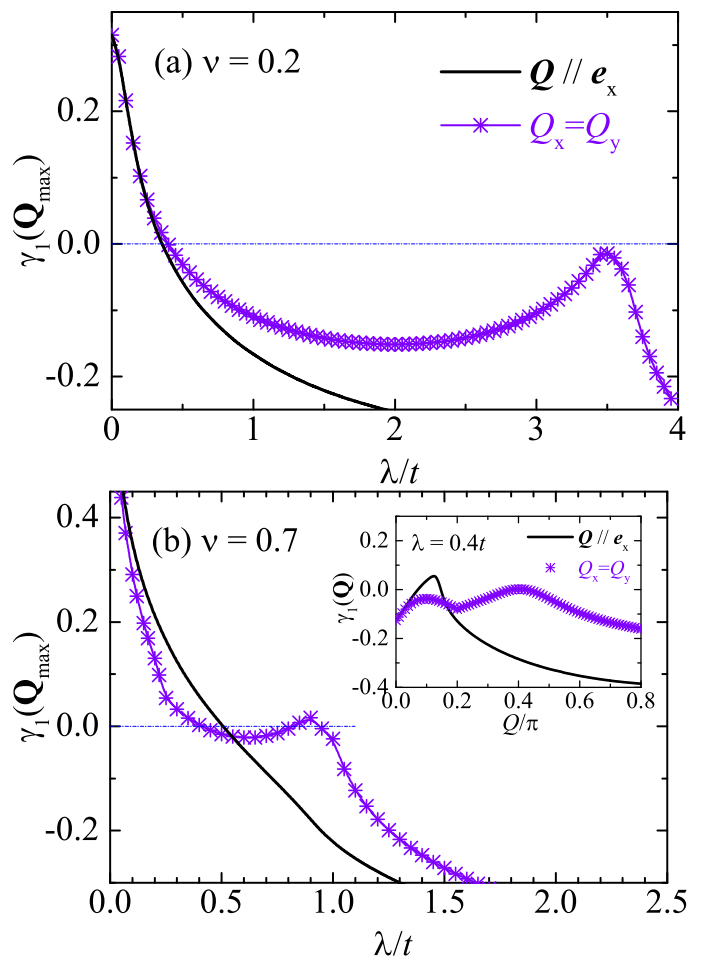


FIG. 7. The peak value of the leading eigenvalue of the inverse vertex function matrix,  $\gamma_1(\mathbf{Q}_{\max})$ , is plotted as a function of the  $d_{x^2-y^2}$ -wave altermagnetic coupling strength  $\lambda$  for two lattice filling factors:  $\nu = 0.2$  (top panel) and  $\nu = 0.7$  (bottom panel). In each panel, the black curve corresponds to the center-of-mass momentum  $\mathbf{Q}$  aligned along the  $x$ -axis, while the violet crosses represent  $\mathbf{Q}$  oriented along the  $x$ -axis or the diagonal ( $Q_x = Q_y$ ). The inset in (b) shows  $\gamma_1(\mathbf{Q})$  for different orientations of  $\mathbf{Q}$ , emphasizing that at small  $d_{x^2-y^2}$ -wave altermagnetic couplings  $\gamma_1(\mathbf{Q}_{\max})$  occurs when  $\mathbf{Q}$  is directed along the  $x$ -axis.

in the nature of the leading pairing instability. To examine this connection, Fig. 6(b) shows the weights of the various pairing channels evaluated precisely at the superfluid-normal phase boundary. Indeed, with increasing  $\nu$  the dominant pairing symmetry evolves from extended  $s$ -wave to  $p$ -wave at  $\nu \simeq 0.3$ , and subsequently to  $d$ -wave at  $\nu \simeq 0.6$ . We emphasize, however, that in the presence of altermagnetism the sub-leading pairing channels remain substantial, particularly near the crossover points at  $\nu \simeq 0.3$  and  $\nu \simeq 0.6$ . Consequently, once the superconducting phase emerges, the pairing order parameter is generally multi-component in nature, incorporating contributions from both spin-singlet and spin-triplet channels.

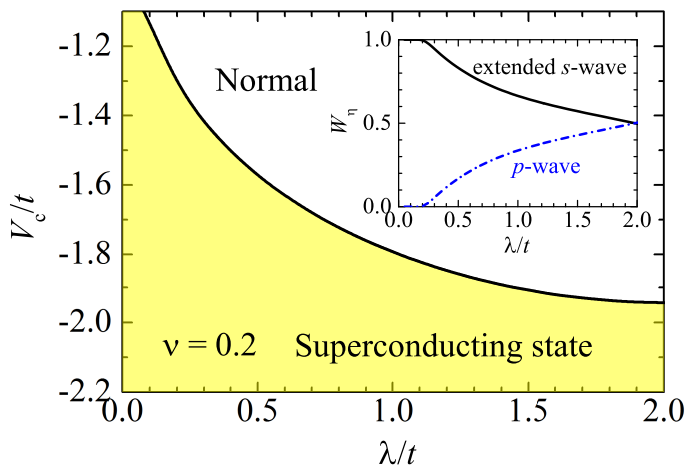


FIG. 8. Phase diagram with  $d_{x^2-y^2}$ -wave altermagnetism: the critical nearest-neighbor interaction strength  $V_c$  is shown as a function of the altermagnetic coupling strength  $\lambda$ , at the lattice filling factor  $\nu = 0.2$ . The inset displays the contributions of different partial-wave components to the dominant pairing channel,  $W_\eta = |M_\eta|^2$ , at the superconducting transition. Here, we take the on-site attraction  $U = -0.01t$ .

### C. $d_{x^2-y^2}$ -wave altermagnetism

We now proceed to analyze the case of  $d_{x^2-y^2}$ -wave altermagnetism. Fig. 7(a) and Fig. 7(b) report  $\gamma_1(\mathbf{Q}_{\max})$  as a function of the altermagnetic coupling  $\lambda$ , at two electron fillings  $\nu = 0.2$  and  $\nu = 0.7$ , respectively. As in the previous analysis, we consider two orientations of the center-of-mass momentum  $\mathbf{Q}$ : aligned either along the  $x$ -axis (black curves) or along the diagonal direction (purple crosses).

For low electron filling ( $\nu = 0.2$ ), we observe that  $\gamma_1(\mathbf{Q}_{\max})$  occurs when  $\mathbf{Q}$  points along the diagonal direction, in clear contrast to the behavior found for  $d_{xy}$ -wave altermagnetism. At higher filling ( $\nu = 0.7$ ), the same tendency persists when the altermagnetic coupling is sufficiently strong. However, for weaker couplings, specifically  $\lambda \leq 0.55t$ , the maximum of  $\gamma_1(\mathbf{Q})$  instead appears  $\mathbf{Q}$  lies along the  $x$ -axis, resembling the behavior characteristic of the  $d_{xy}$ -wave case. This re-orientation of the optimal momentum  $\mathbf{Q}$  is most clearly illustrated by examining the  $Q$ -dependence of  $\gamma_1(\mathbf{Q})$  at a relatively small coupling  $\lambda = 0.4t$ , as shown in the inset of Fig. 7(b). In this regime, we typically find a single peak when  $\mathbf{Q}$  is directed along the  $x$ -axis, whereas a double-peak structure emerges when  $\mathbf{Q}$  lies along the diagonal. In general, the single peak in the former configuration competes with the outer peak of the doublet in the latter, and becomes energetically favorable at weaker altermagnetic coupling.

In contrast to the  $d_{xy}$ -wave altermagnetism, a notable feature of  $d_{x^2-y^2}$ -wave altermagnetism is that  $\gamma_1(\mathbf{Q}_{\max})$  does not decrease monotonically as the altermagnetic coupling  $\lambda$  increases. Instead, we typically observe the emergence of a local maximum at relatively large  $\lambda$ , whose position depends sensitively on the electron filling.

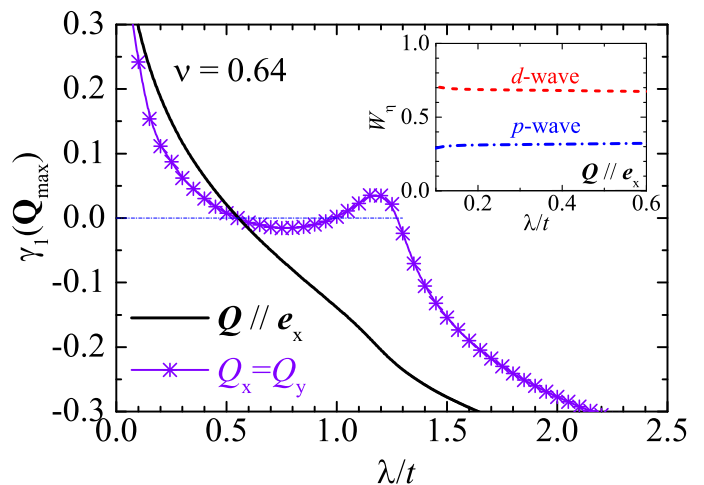


FIG. 9. Analysis of the pairing instability under the high-electron density conditions of Ref. <sup>45</sup>. At a large electron filling factor  $\nu = 0.64$  and nearest-neighbor interaction  $V = -1.6t$ , the maximum of the leading eigenvalue of the inverse vertex function matrix  $\gamma_1(\mathbf{Q})$  at small  $d_{x^2-y^2}$ -wave altermagnetic couplings occurs when the center-of-mass momentum  $\mathbf{Q}$  is aligned along the  $x$ -axis. The inset shows how the weights of the different partial-wave components  $W_\eta = |M_\eta|^2$  vary with the altermagnetic coupling strength  $\lambda$ .

This unexpected enhancement can likely be attributed to a nesting effect when  $\mathbf{Q}$  lies along the diagonal direction. In general, the optimal magnitude of  $\mathbf{Q}$  scales approximately with the altermagnetic coupling strength  $\lambda$ , remaining small for small  $\lambda$  and becoming large for large  $\lambda$ . However, because of band nesting, both  $\mathbf{Q} = (q, q)$  and  $\tilde{\mathbf{Q}} = (\pi - q, \pi - q)$  can be equally favorable as optimal momenta. This indicates that the pairing tendency may persist even at strong altermagnetic coupling. As a consequence, in the very low-filling limit, a local maximum of  $\gamma_1(\mathbf{Q})$  appears around  $\lambda = 4t$ . As the filling increases, this maximum shifts progressively toward smaller values of  $\lambda$ .

In Fig. 8, we present the phase diagram obtained by varying the altermagnetic coupling strength at a fixed low electron filling  $\nu = 0.2$ . The critical nearest-neighbor attraction  $V_c$ , required to drive the system into the superconducting phase, generally decreases as the altermagnetic coupling increases. As illustrated in the inset, the dominant pairing channel at weak altermagnetic coupling is the extended  $s$ -wave, consistent with the low filling regime. However, as the coupling strength increases up to  $\lambda = 2t$ , the sub-leading  $p$ -wave channel gradually becomes more prominent and eventually reaches a magnitude comparable to that of the extended  $s$ -wave component. As in the case of  $d_{xy}$ -wave altermagnetism, the superconducting order parameter in this regime is therefore also multi-component in character, comprising contributions from both spin-singlet and spin-triplet channels.

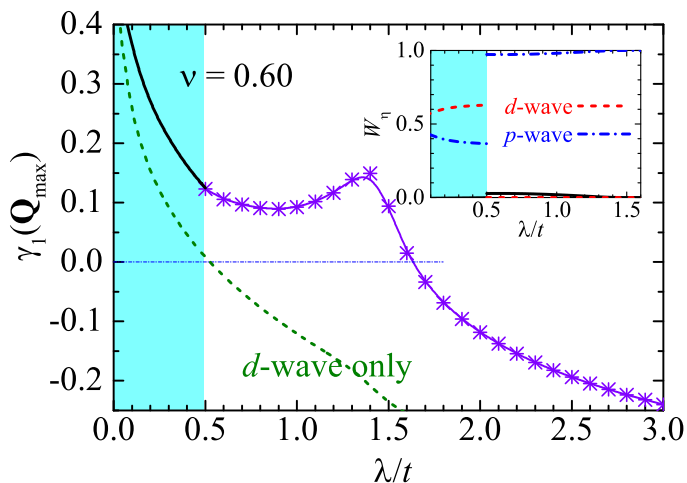


FIG. 10. Analysis of the pairing instability under the conditions of Ref.<sup>31</sup>, for a filling factor  $\nu = 0.6$  and nearest-neighbor interaction  $V = -2.0t$ .  $\gamma_1(\mathbf{Q}_{\max})$  is plotted against the  $d_{x^2-y^2}$ -wave altermagnetic coupling strength  $\lambda$ , alongside the result obtained by considering only the  $d$ -wave pairing channel (green dashed line) as assumed in Ref.<sup>31</sup>. The inset illustrates how the weights of the various partial-wave components  $W_n = |M_n|^2$  change with  $\lambda$ .

## V. POTENTIAL CONNECTIONS TO PREVIOUS WORK

Most recently, Jasiewicz *et al.* carried out a mean-field study of the FFLO superconducting state with a nearest-neighbor attraction  $V = -1.6t$  in the presence of  $d_{x^2-y^2}$ -wave altermagnetism<sup>45</sup>. At a relatively high electron filling,  $\nu = 0.64$ , they identified a singlet-triplet mixed Fulde-Ferrell (FF) order parameter characterized by a dominant  $d$ -wave component and a sub-leading  $p$ -wave component, emerging when the altermagnetic coupling strength satisfies  $\lambda \gtrsim 0.24t$  and the center-of-mass  $\mathbf{Q}$  is aligned along the  $x$ -axis<sup>45</sup>. Under identical conditions, we have performed an analysis of the leading pairing instability. As shown in Fig. 9, the superconducting transition indeed sets in for  $\lambda < 0.55t$  and  $\mathbf{Q}$  oriented along the  $x$ -axis, and the resulting state contains both  $d$ -wave and  $p$ -wave pairing components (see inset). Furthermore, the ratio between these two components (approximately 2 : 1) is consistent with the relative magnitudes of the pairing amplitudes reported by Jasiewicz *et al.* (see Fig. 10(d) of Ref.<sup>45</sup>).

In another theoretical work<sup>31</sup>, Chakraborty and Black-Schaffer investigated the FFLO state at the nearest-neighbor attraction  $V = -2t$ , again with  $d_{x^2-y^2}$ -wave altermagnetism. Restricting their analysis to the singlet pairing channel and considering an electron filling of  $\nu = 0.6$ , they found an altermagnetism-driven FF state within the window  $0.44t \leq \lambda \leq 0.56t$ <sup>31</sup>. In Fig. 10, we have revisited this singlet channel approximation, by benchmarking it against our full channel calculations. When only the  $d$ -wave channel is retained, we obtain

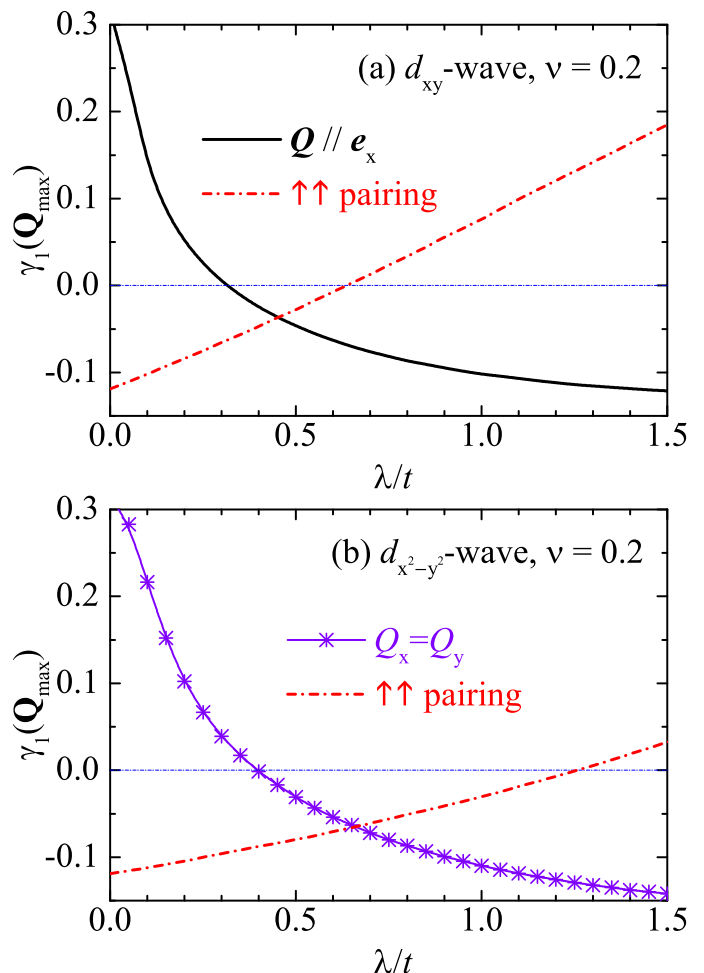


FIG. 11. The peak value of the leading eigenvalue of the inverse vertex function matrix  $\gamma_1(\mathbf{Q}_{\max})$  at the lattice filling factor  $\nu = 0.2$  is shown for (a)  $d_{xy}$ -wave and (b)  $d_{x^2-y^2}$ -wave altermagnetism. Results for the  $\uparrow\downarrow$  pairing (black curve in (a) or the line with crosses in (b)) are compared with those for the triplet  $\uparrow\uparrow$  pairing (red dot-dashed line). Here, we set  $V = V_\sigma = -1.5t$ .

a critical altermagnetic coupling  $\lambda_c \simeq 0.56t$ , consistent with the finding by Chakraborty *et al.*<sup>31</sup>. However, this value is substantially smaller than the critical coupling  $\lambda_c \simeq 1.63t$  obtained from the full channel calculation. Actually, as indicated in the inset, the  $p$ -wave pairing channel remains significant throughout. For  $\lambda \gtrsim 0.5t$ , it becomes nearly the sole dominant pairing channel.

## VI. CONSIDERATIONS ON PARALLEL-SPIN PAIRING

Up to this point, we have concentrated on pairing between two electrons with opposite spins, motivated by the argument illustrated in Fig. 2 that parallel-spin pairing is not the dominant instability when  $|V_\sigma| \leq |V|$  in the regime of sufficiently weak altermagnetism. We now ex-

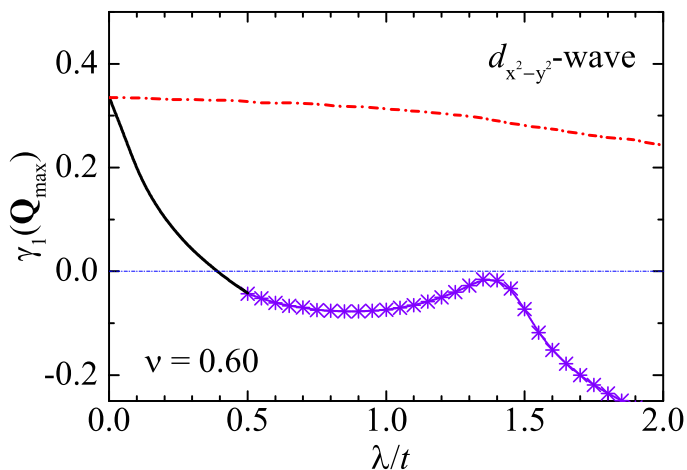


FIG. 12. The same as in Fig. 11(b), except evaluated for a lattice filling factor of  $\nu = 0.6$ .

amine more carefully the specific conditions that arise when the nearest-neighbor attractive interactions have equal strength,  $V_\sigma = V$ .

In Fig. 11, for low electron filling  $\nu = 0.2$ , we compare the  $\lambda$ -dependence of  $\gamma_1(\mathbf{Q}_{\max})$  for both anti-parallel-spin pairing and parallel-spin pairing, in the presence of either  $d_{xy}$ -wave (a) or  $d_{x^2-y^2}$ -wave (b) altermagnetism. For parallel-spin pairing, the instability always occurs at  $\mathbf{Q} = 0$  (not shown), regardless of whether altermagnetism is present. Moreover, as the altermagnetic coupling  $\lambda$  increases, the leading eigenvalue  $\gamma_1(\mathbf{Q}_{\max})$  tends to increase rather than decrease. Consequently, at sufficiently large altermagnetic coupling, the dominant pairing instability eventually shifts from anti-parallel-spin pairing to parallel-spin pairing. However, for altermagnetic coupling below the critical value  $\lambda_c$ , the leading pairing instability consistently arises from electrons with anti-parallel spins. Therefore, the phase diagrams shown in Fig. 6(a) and Fig. 8 remain valid in the regime of weak altermagnetic coupling.

This behavior changes at higher electron fillings. As illustrated in Fig. 12, taking  $d_{x^2-y^2}$ -wave altermagnetism as a representative example, at electron filling  $\nu = 0.6$  the leading pairing instability now occurs among electrons with same spins at all altermagnetic couplings. This parallel-spin, triplet pairing state has recently been explored in the literature, both in the presence<sup>27</sup> and absence<sup>38</sup> of spin-orbit coupling.

## VII. CONCLUSIONS AND OUTLOOKS

In summary, we have investigated the pairing instability in an altermagnetic metal subject to a finite-range attractive interaction that accommodates multiple pairing channels with distinct parity and symmetry. The system is described by an altermagnetic Hubbard  $UV$  model incorporating both on-site ( $U$ ) and nearest-neighbor ( $V$ )

attractive interactions. Within the standard non-self-consistent many-body  $T$ -matrix approximation<sup>73</sup>, we have determined the two-particle vertex function by projecting it onto the different pairing channels. By subsequently diagonalizing the resulting inverse vertex matrix, we have identified the leading pairing instability according to the well-established Thouless criterion<sup>68,69</sup>.

In this way, we have confirmed the emergence of altermagnetism-driven FFLO superconducting states, which have already been examined in some detail in earlier works<sup>25,30,31,38,40,41,44</sup>. Our systematic analysis of the pairing instability, however, goes beyond the commonly adopted single-pairing-channel approximation and demonstrates that finite-momentum pairing naturally leads to the admixture of multiple pairing channels with different parity. Consequently, altermagnetic FFLO states generally exhibit a multi-component order parameter containing both spin-singlet and spin-triplet contributions<sup>45</sup>. At low electron filling, this result is consistent with the previous exact two-electron calculation<sup>48</sup>, which predicts finite-momentum bound pairs with mixed singlet-triplet character.

It would be of considerable interest to examine our predictions in altermagnetic superconductors, which have not yet been experimentally realized. In such prospective systems, effective nearest-neighbor attractive interactions may emerge from strong on-site Coulomb repulsion through altermagnetic spin fluctuations<sup>72,74-77</sup>. More realistic theoretical analyses, incorporating spin-fluctuation-mediated pairing mechanisms, will be pursued in future work.

In the mixed singlet-triplet superconducting phase, it is also important to investigate the role of relative phases between different components of the order parameter. The breaking of time-reversal symmetry can give rise to spontaneous surface currents, similar to those found in topological insulators, and this effect has already been discussed for the  $s + id_{xy}$  spin-singlet state<sup>78</sup>. Extending the analysis from multi-component singlet-singlet pairing to the singlet-triplet case presents an interesting and worthwhile direction for further study.

## ACKNOWLEDGMENTS

This research was supported by the Australian Research Council's (ARC) Discovery Program, Grants Nos. DP240101590 (H.H.), FT230100229 (J.W.) and DP240100248 (X.-J.L.).

### Appendix A: Numerical calculation of the pair propagator matrix

In evaluating the pair propagator matrix Eq. (19), it is necessary to eliminate the sharp structure in the integrand that arises when the energy  $\omega$  lies within the two-electron continuum. To address this issue, we intro-

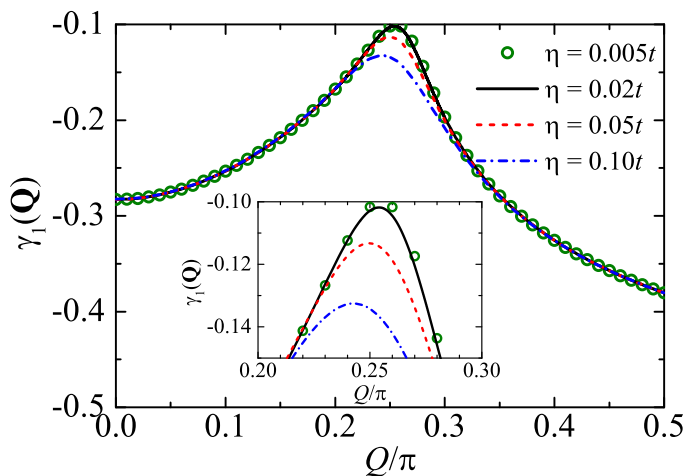


FIG. 13. The dependence of the largest eigenvalue of the inverse vertex function matrix  $\gamma_1(\mathbf{Q})$  on the spectral broadening factor  $\eta$ :  $\eta = 0.005t$  (circles),  $\eta = 0.02t$  (black solid line),  $\eta = 0.05t$  (red dashed line) and  $\eta = 0.10t$  (blue dot-dashed line). The inset zooms in on the region near the peak. Results are shown for  $d_{xy}$ -wave altermagnetism with coupling strength  $\lambda = 1.0t$  and filling factor  $\nu = 0.2$ . Other parameters are  $U = -0.01t$  and  $V = -1.5t$ .

duce a small spectral broadening factor  $\eta > 0$  by shifting the energy as,  $\omega \rightarrow \omega + i\eta$ . We then extrapolate to the zero-broadening limit  $\eta = 0^+$  by using a cubic polynomial fitting.

Fig. 13 presents an example for  $d_{xy}$ -wave altermagnetism with coupling strength  $\lambda = 1.0t$  and low electron filling  $\nu = 0.2$ . The leading eigenvalue of the inverse vertex function matrix,  $\gamma_1(\mathbf{Q} = Q\mathbf{e}_x)$ , is shown for several values of the spectral broadening factor  $\eta$ , as indicated. Although the cubic fitting procedure does not completely eliminate the  $\eta$ -dependence, the remaining dependence becomes negligible for sufficiently small  $\eta$ . Throughout this work, we typically take  $\eta = 0.02t$ . The estimated absolute error in the leading eigenvalue is on the order of  $10^{-3}t^{-1}$ , which is barely discernible in the figure.

### Appendix B: The effect of on-site attractive interactions

Here, we briefly discuss how the pairing instability is modified by incorporating an on-site attractive interac-

tion. In Fig. 14, we report  $\gamma_1(\mathbf{Q}_{\max})$  both in the absence and presence of on-site attraction, under  $d_{xy}$ -wave altermagnetism. As shown in the inset, the peak center-of-mass momentum  $\mathbf{Q}$  remains nearly independent of the strength of the on-site attraction. In contrast, the critical altermagnetic coupling strength  $\lambda_c$  increases substantially when the on-site attraction is included, as indicated by the red arrow in the figure.

In Fig. 15(a), we present the resulting critical altermagnetic coupling  $\lambda_c$  as a function of the on-site attraction, which defines the corresponding phase diagram.

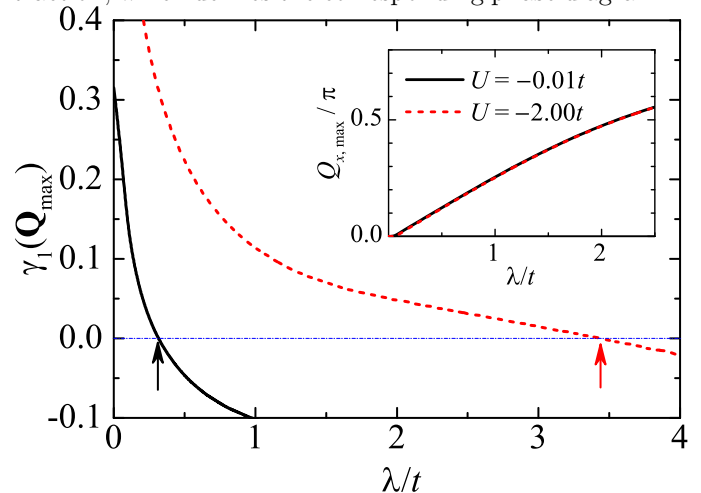


FIG. 14. The maximum value of the leading eigenvalue of the inverse vertex function matrix  $\gamma_1(\mathbf{Q}_{\max})$  is shown as a function of the  $d_{xy}$ -wave altermagnetic coupling strength  $\lambda$  for two different on-site attractive interactions:  $U = -0.01t$  (black curve) and  $U = -2.00t$  (red dashed line). The inset shows the magnitude of the center-of-mass momentum  $\mathbf{Q}$  at which this maximum occurs, with  $\mathbf{Q}$  oriented along the  $x$ -axis. The nearest-neighbor interaction strength is  $V = -1.5t$  and the electron filling is  $\nu = 0.2$ .

Fig. 15(b) further displays the contributions of different partial-wave components to the emerging superconducting order parameter at the phase transition. As the on-site attraction becomes stronger, the purely  $s$ -wave component is progressively enhanced. At about  $U \simeq -1.75t \sim V$ , it exceeds the extended  $s$ -wave contribution and eventually becomes the dominant pairing channel, as expected.

\* hhu@swin.edu.au

† yohashi@keio.jp

<sup>1</sup> L. Šmejkal, J. Sinova, and T. Jungwirth, Emerging Research Landscape of Altermagnetism, *Phys. Rev. X* **12**, 040501 (2022).

<sup>2</sup> L. Bai, W. Feng, S. Liu, L. Šmejkal, Y. Mokrousov, and Y. Yao, Altermagnetism: exploring new frontiers in mag-

netism and spintronics, *Adv. Func. Mater.* **34**, 2409327 (2024).

<sup>3</sup> T. Jungwirth, R. M. Fernandes, E. Fradkin, A. H. MacDonald, J. Sinova, and L. Šmejkal, Altermagnetism: an unconventional spin-ordered phase of matter, *Newton* **1**, 100162 (2025).

<sup>4</sup> Z. Liu, H. Hu, and X.-J. Liu, Altermagnetism and super-

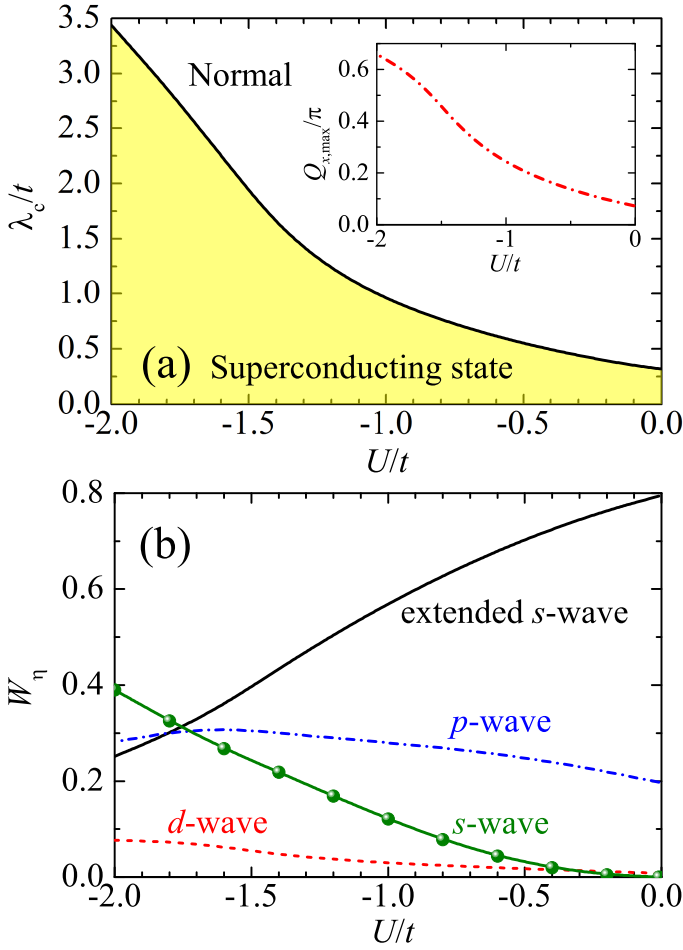


FIG. 15. (a) Phase diagram for  $d_{xy}$ -wave altermagnetism as a function of on-site attraction: the critical altermagnetic coupling strength  $\lambda_c$  is plotted against the on-site attractive interaction strength  $U$ . The inset depicts the center-of-mass momentum  $\mathbf{Q} = Q\mathbf{e}_x$  at the superconducting phase boundary. (b) The contributions of different partial-wave components to the dominant pairing channel  $W_\eta = |M_\eta|^2$  at the superconducting transition. The nearest-neighbor interaction strength is  $V = -1.5t$  and the electron filling is  $\nu = 0.2$ .

conductivity: A short historical review, arXiv:2510.09170 (2025).

- <sup>5</sup> Y. Noda, K. Ohno, and S. Nakamura, Momentum-dependent band spin splitting in semiconducting  $\text{MnO}_2$ : a density functional calculation, *Phys. Chem. Chem. Phys.* **18**, 13294 (2016).
- <sup>6</sup> M. Naka, S. Hayami, H. Kusunose, Y. Yanagi, Y. Motome, and H. Seo, Spin current generation in organic antiferromagnets, *Nat. Commun.* **10**, 4305 (2019).
- <sup>7</sup> S. Hayami, Y. Yanagi, and H. Kusunose, Momentum-Dependent Spin Splitting by Collinear Antiferromagnetic Ordering, *J. Phys. Soc. Jpn.* **88**, 123702 (2019).
- <sup>8</sup> K.-H. Ahn, A. Hariki, K.-W. Lee, and J. Kuneš, Antiferromagnetism in  $\text{RuO}_2$  as  $d$ -wave Pomeranchuk instability, *Phys. Rev. B* **99**, 184432 (2019).
- <sup>9</sup> S. Hayami, Y. Yanagi, and H. Kusunose, Bottom-up design of spin-split and reshaped electronic band structures in antiferromagnets without spin-orbit coupling: Procedure

- on the basis of augmented multipoles, *Phys. Rev. B* **102**, 144441 (2020).
- <sup>10</sup> L. Šmejkal, R. González-Hernández, T. Jungwirth, and J. Sinova, Crystal time-reversal symmetry breaking and spontaneous Hall effect in collinear antiferromagnets, *Sci. Adv.* **6**, eaaz8809 (2020).
- <sup>11</sup> I. I. Mazin, K. Koepf, M. D. Johannes, R. González-Hernández, and L. Šmejkal, Prediction of unconventional magnetism in doped  $\text{FeSb}_2$ , *Proc. Natl. Acad. Sci. U.S.A.* **118**, e2108924118 (2021).
- <sup>12</sup> I. I. Mazin, Altermagnetism in  $\text{MnTe}$ : Origin, predicted manifestations, and routes to detwinning, *Phys. Rev. B* **107**, L100418 (2023).
- <sup>13</sup> P. A. McClarty and J. G. Rau, Landau Theory of Altermagnetism, *Phys. Rev. Lett.* **132**, 176702 (2024).
- <sup>14</sup> M. Roig, A. Kreisel, Y. Yu, B. M. Andersen, and D. F. Agterberg, Minimal models for altermagnetism, *Phys. Rev. B* **110**, 144412 (2024).
- <sup>15</sup> Z. Xiao, J. Zhao, Y. Li, R. Shindou, and Z.-D. Song, Spin space groups: full classification and applications, *Phys. Rev. X* **14**, 031037 (2024).
- <sup>16</sup> X. Chen, J. Ren, Y. Zhu, Y. Yu, A. Zhang, P. Liu, J. Li, Y. Liu, C. Li, and Q. Liu, Enumeration and representation theory of spin space groups, *Phys. Rev. X* **14**, 031038 (2024).
- <sup>17</sup> Y. Jiang, Z. Song, T. Zhu, Z. Fang, H. Weng, Z.-X. Liu, J. Yang, and C. Fang, Enumeration of spin-space groups: towards a complete description of symmetries of magnetic orders, *Phys. Rev. X* **14**, 031039 (2024).
- <sup>18</sup> J. Krempaský, L. Šmejkal, S. W. D'Souza, M. Hajlaoui, G. Springholz, K. Uhlířová, F. Alarab, P. C. Constantinou, V. Strocov, D. Usanov, W. R. Pudelko, R. González-Hernández, A. Birk Hellenes, Z. Jansa, H. Reichlová, Z. Šobáň, R. D. Gonzalez Betancourt, P. Wadley, J. Sinova, D. Kriegner, J. Minár, J. H. Dil, and T. Jungwirth, Altermagnetic lifting of Kramers spin degeneracy, *Nature (London)* **626**, 517 (2024).
- <sup>19</sup> O. J. Amin, A. Dal Din, E. Golias, Y. Niu, A. Zakharov, S. C. Fromage, C. J. B. Fields, S. L. Heywood, R. B. Cousins, F. Maccherozzi, J. Krempaský, J. H. Dil, D. Kriegner, B. Kiraly, R. P. Campion, A. W. Rushforth, K. W. Edmonds, S. S. Dhesi, L. Šmejkal, T. Jungwirth, and P. Wadley, Nanoscale imaging and control of altermagnetism in  $\text{MnTe}$ , *Nature (London)* **636**, 348 (2024).
- <sup>20</sup> B. Jiang, M. Hu, J. Bai, Z. Song, C. Mu, G. Qu, W. Li, W. Zhu, H. Pi, Z. Wei, Y. Sun, Y. Huang, X. Zheng, Y. Peng, L. He, S. Li, J. Luo, Z. Li, G. Chen, H. Li, H. Weng, and T. Qian, A metallic room-temperature d-wave altermagnet. *Nat. Phys.* **21**, 754 (2025).
- <sup>21</sup> F. Zhang, X. Cheng, Z. Yin, C. Liu, L. Deng, Y. Qiao, Z. Shi, S. Zhang, J. Lin, Z. Liu, M. Ye, Y. Huang, X. Meng, C. Zhang, T. Okuda, K. Shimada, S. Cui, Y. Zhao, G.-H. Cao, S. Qiao, J. Liu, and C. Chen, Crystal-symmetry-paired spin-valley locking in a layered room-temperature metallic altermagnet candidate. *Nat. Phys.* **21**, 760 (2025).
- <sup>22</sup> I. I. Mazin, Notes on altermagnetism and superconductivity, *AAPPS Bull.* **35**, 8 (2025).
- <sup>23</sup> Y. Fukaya, B. Lu, K. Yada, Y. Tanaka, and J. Cayao, Superconducting phenomena in systems with unconventional magnets, *J. Phys.: Condens. Matter* **37**, 313003 (2025).
- <sup>24</sup> J. A. Ouassou, A. Brataas, and J. Linder, dc Josephson effect in altermagnets, *Phys. Rev. Lett.* **131**, 076003 (2023).
- <sup>25</sup> S. Sumita, M. Naka, and H. Seo, Fulde-Ferrell-Larkin-Ovchinnikov state induced by antiferromagnetic order in  $\kappa$ -

- type organic conductors, *Phys. Rev. Res.* **5**, 043171 (2023).
- <sup>26</sup> C. Sun, A. Brataas, and J. Linder, Andreev reflection in altermagnets, *Phys. Rev. B* **108**, 054511 (2023).
- <sup>27</sup> D. Zhu, Z.-Y. Zhuang, Z. Wu, and Z. Yan, Topological superconductivity in two-dimensional altermagnetic metals, *Phys. Rev. B* **108**, 184505 (2023).
- <sup>28</sup> B. Brekke, A. Brataas, and A. Sudbø, Two-dimensional altermagnets: superconductivity in a minimal microscopic model, *Phys. Rev. B* **108**, 224421 (2023).
- <sup>29</sup> B. Lu, K. Maeda, H. Ito, K. Yada, and Y. Tanaka,  $\varphi$  Josephson Junction Induced by Altermagnetism, *Phys. Rev. Lett.* **133**, 226002 (2024).
- <sup>30</sup> S.-B. Zhang, L.-H. Hu, and T. Neupert, Finite-momentum Cooper pairing in proximitized altermagnets, *Nat. Commun.* **15**, 1801 (2024).
- <sup>31</sup> D. Chakraborty and A. M. Black-Schaffer, Zero-field finite-momentum and field-induced superconductivity in altermagnets, *Phys. Rev. B* **110**, L060508 (2024).
- <sup>32</sup> A. Mæland, B. Brekke, and A. Sudbø, Many-body effects on superconductivity mediated by double-magnon processes in altermagnets, *Phys. Rev. B* **109**, 134515 (2024).
- <sup>33</sup> A. Bose, S. Vadnais, and A. Paramakanti, Altermagnetism and superconductivity in a multiorbital  $t - J$  model, *Phys. Rev. B* **110**, 205120 (2024).
- <sup>34</sup> V. S. de Carvalho and H. Freire, Unconventional superconductivity in altermagnets with spin-orbit coupling, *Phys. Rev. B* **110**, L220503 (2024).
- <sup>35</sup> D. Chakraborty and A. M. Black-Schaffer, Perfect superconducting diode effect in altermagnets, *Phys. Rev. Lett.* **135**, 026001 (2025).
- <sup>36</sup> K. Mukasa and Y. Masaki, Finite-momentum Superconductivity in Two-dimensional Altermagnets with a Rashba-type Spin-Orbit Coupling, *J. Phys. Soc. Jpn.* **94**, 064705 (2025).
- <sup>37</sup> G. Sim and J. Knolle, Pair Density Waves and Supercurrent Diode Effect in Altermagnets, *Phys. Rev. B* **112**, L020502 (2025).
- <sup>38</sup> S. Hong, M. J. Park, and K.-M. Kim, Unconventional  $p$ -wave and finite-momentum superconductivity induced by altermagnetism through the formation of Bogoliubov Fermi surface, *Phys. Rev. B* **111**, 054501 (2025).
- <sup>39</sup> Y. Fukaya, K. Maeda, K. Yada, J. Cayao, Y. Tanaka, and B. Lu, Josephson effect and odd-frequency pairing in superconducting junctions with unconventional magnets, *Phys. Rev. B* **111**, 064502 (2025).
- <sup>40</sup> S. Sumita, M. Naka, and H. Seo, Phase-modulated superconductivity via altermagnetism, *Phys. Rev. B* **112**, 144510 (2025).
- <sup>41</sup> H. Hu, Z. Liu, and X.-J. Liu, Unconventional superconductivity of an altermagnetic metal: Polarized BCS and inhomogeneous FFLO states, *Phys. Rev. B* **112**, 184501 (2025).
- <sup>42</sup> I. V. Iorsh, Electron pairing by dispersive phonons in altermagnets: Reentrant superconductivity and continuous transition to finite momentum superconducting state, *Phys. Rev. B* **111**, L220503 (2025).
- <sup>43</sup> H. Hu and X.-J. Liu, Quantum Lifshitz points in an altermagnetic superconductor, *AAPPS Bull.* **35**, 35 (2025).
- <sup>44</sup> Z. Liu, H. Hu, and X.-J. Liu, Fulde-Ferrell-Larkin-Ovchinnikov states and topological Bogoliubov Fermi surfaces in altermagnets: an analytical study, *Phys. Rev. B* **113**, 024518 (2026).
- <sup>45</sup> K. Jasiewicz, P. Wójcik, M. Nowak, and M. Zegrodnik, Interplay between altermagnetism and superconductivity in two dimensions: intertwined symmetries and singlet-triplet mixing, arXiv:2511.05190.
- <sup>46</sup> P.-H. Fu, S. Mondal, J.-F. Liu, Y. Tanaka, and J. Cayao, Floquet Engineering Spin Triplet States in Unconventional Magnets, *Phys. Rev. Lett.* **136**, 066703 (2026).
- <sup>47</sup> X.-J. Liu and H. Hu, Altermagnetism-driven FFLO superconductivity in finite-filling 2D lattices, arXiv:2601.06735.
- <sup>48</sup> H. Hu, Z. Liu, J. Wang, and X.-J. Liu, Finite-momentum bound pairs of two electrons in an altermagnetic metal, arXiv:2601.12905.
- <sup>49</sup> K. Monkman, J. Weng, N. Heinsdorf, A. Nocera, and M. Franz, Persistent spin currents in superconducting altermagnets, arXiv:2507.22139.
- <sup>50</sup> P. Fulde and R. A. Ferrell, Superconductivity in a Strong Spin-Exchange Field, *Phys. Rev.* **135**, A550 (1964).
- <sup>51</sup> A. I. Larkin and Yu. N. Ovchinnikov, Nonuniform state of superconductors, *Zh. Eksp. Teor. Fiz.* **47**, 1136 (1964) [*Sov. Phys. JETP* **20**, 762 (1965)].
- <sup>52</sup> R. Casalbuoni and G. Nardulli, Inhomogeneous superconductivity in condensed matter and QCD, *Rev. Mod. Phys.* **76**, 263 (2004).
- <sup>53</sup> H. Hu and X.-J. Liu, Mean-field phase diagrams of imbalanced Fermi gases near a Feshbach resonance, *Phys. Rev. A* **73**, 051603(R) (2006).
- <sup>54</sup> H. Hu, X.-J. Liu, and P. D. Drummond, Phase Diagram of a Strongly Interacting Polarized Fermi Gas in One Dimension, *Phys. Rev. Lett.* **98**, 070403 (2007).
- <sup>55</sup> X.-J. Liu, H. Hu, and P. D. Drummond, Fulde-Ferrell-Larkin-Ovchinnikov states in one-dimensional spin-polarized ultracold atomic Fermi gases, *Phys. Rev. A* **76**, 043605 (2007).
- <sup>56</sup> L. Radzihovsky and D. E. Sheehy, Imbalanced Feshbach-resonant Fermi gases, *Rep. Prog. Phys.* **73**, 076501 (2010).
- <sup>57</sup> K. B. Gubbels and H. T. C. Stoof, Imbalanced Fermi gases at unitarity, *Phys. Rep.* **525**, 255 (2013).
- <sup>58</sup> X.-J. Liu and H. Hu, Inhomogeneous Fulde-Ferrell superfluidity in spin-orbit-coupled atomic Fermi gases, *Phys. Rev. A* **87**, 051608(R) (2013).
- <sup>59</sup> Y. Cao, S.-H. Zou, X.-J. Liu, S. Yi, G.-L. Long, and H. Hu, Gapless Topological Fulde-Ferrell Superfluidity in Spin-Orbit Coupled Fermi Gases, *Phys. Rev. Lett.* **113**, 115302 (2014).
- <sup>60</sup> D. E. Sheehy, Fulde-Ferrell-Larkin-Ovchinnikov state of two-dimensional imbalanced Fermi gases, *Phys. Rev. A* **92**, 053631 (2015).
- <sup>61</sup> J. Wang, Y. Che, L. Zhang, and Q. Chen, Instability of Fulde-Ferrell-Larkin-Ovchinnikov states in atomic Fermi gases in three and two dimensions, *Phys. Rev. B* **97**, 134513 (2018).
- <sup>62</sup> T. Kawamura and Y. Ohashi, Feasibility of a Fulde-Ferrell-Larkin-Ovchinnikov superfluid Fermi atomic gas, *Phys. Rev. A* **106**, 033320 (2022).
- <sup>63</sup> T. Kawamura and Y. Ohashi, Non-equilibrium BCS-BEC crossover and unconventional FFLO superfluid in a strongly interacting driven-dissipative Fermi gas, *AAPPS Bull.* **34**, 31 (2024).
- <sup>64</sup> S. Uji, T. Terashima, M. Nishimura, Y. Takahide, T. Konoike, K. Enomoto, H. Cui, H. Kobayashi, A. Kobayashi, H. Tanaka, M. Tokumoto, E. S. Choi, T. Tokumoto, D. Graf, and J. S. Brooks, Vortex Dynamics and the Fulde-Ferrell-Larkin-Ovchinnikov State in a Magnetic-Field-Induced Organic Superconductor, *Phys. Rev. Lett.* **97**, 157001 (2006).
- <sup>65</sup> Y.-A. Liao, A. S. C. Rittner, T. Paprotta, W. Li, G. B.

- Partridge, R. G. Hulet, S. K. Baur, and E. J. Mueller, *Nature* (London) **467**, 567 (2010).
- <sup>66</sup> D. Zhao, L. Debbeler, M. Kühne, S. Fecher, N. Gross, and J. Smet, Evidence of finite-momentum pairing in a centrosymmetric bilayer, *Nature Phys.* **19**, 1599 (2023).
- <sup>67</sup> R. Soto-Garrido and E. Fradkin, Pair-density-wave superconducting states and electronic liquid-crystal phases, *Phys. Rev. B* **89**, 165126 (2014).
- <sup>68</sup> D. J. Thouless, Perturbation theory in statistical mechanics and the theory of superconductivity, *Ann. Phys. (N. Y.)* **10**, 553 (1960).
- <sup>69</sup> X.-J. Liu and H. Hu, BCS-BEC crossover in an asymmetric two-component Fermi gas, *Europhys. Lett.* **75**, 364 (2006).
- <sup>70</sup> L. N. Cooper, Bound Electron Pairs in a Degenerate Fermi Gas, *Phys. Rev.* **104**, 1189 (1956).
- <sup>71</sup> J. E. Hirsch, Attractive Interaction and Pairing in Fermion Systems with Strong On-Site Repulsion, *Phys. Rev. Lett.* **54**, 1317 (1985).
- <sup>72</sup> D. J. Scalapino, E. Loh, Jr., and J. E. Hirsch, *d*-wave pairing near a spin-density-wave instability, *Phys. Rev. B* **34**, 8190(R) (1986).
- <sup>73</sup> G. D. Mahan, *Many-Particle Physics*, 3rd ed. (Springer, New York, 2000).
- <sup>74</sup> Y. Ohashi and H. Shiba, Pairing and Depairing Effects of Antiferromagnetic Spin Fluctuations in High-Tc Superconductivity, *J. Phys. Soc. Jpn.* **62**, 2783 (1993).
- <sup>75</sup> A. T. Rømer, A. Kreisel, I. Eremin, M. A. Malakhov, T. A. Maier, P. J. Hirschfeld, and B. M. Andersen, Pairing symmetry of the one-band Hubbard model in the paramagnetic weak-coupling limit: A numerical RPA study, *Phys. Rev. B* **92**, 104505 (2015).
- <sup>76</sup> Y.-M. Wu, Y. Wang, and R. M. Fernandes, Intra-unit-cell singlet pairing mediated by altermagnetic fluctuations, *Phys. Rev. Lett.* **135**, 156001 (2025).
- <sup>77</sup> N. Parthenios, P. M. Bonetti, R. González-Hernández, W. H. Campos, L. Šmejkal, and L. Classen, Spin and pair density waves in two-dimensional altermagnetic metals, *Phys. Rev. B* **112**, 214410 (2025).
- <sup>78</sup> Y. Kusama and Y. Ohashi, Effect of the BCS supercurrent on the spontaneous surface flow in unconventional superconductivity with broken time-reversal-symmetry, *J. Phys. Soc. Jpn.* **68**, 987 (1999).